Additive Manufacturing: Metallurgy, Cut Analysis & Porosity

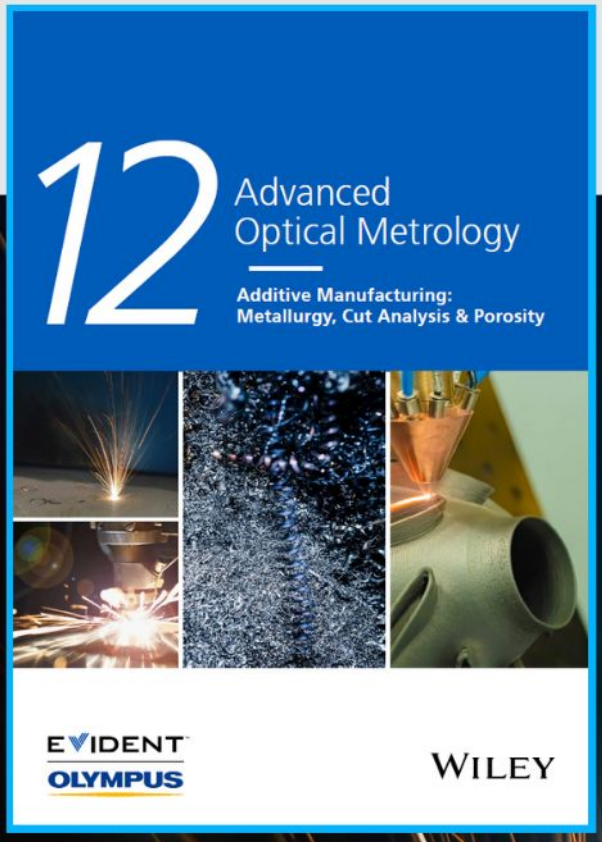

The latest eBook from Advanced Optical Metrology. Download for free.

In industry, sector after sector is moving away from conventional production methods to additive manufacturing, a technology that has been recommended for substantial research investment.

Download the latest eBook to read about the applications, trends, opportunities, and challenges around this process, and how it has been adapted to different industrial sectors.

EVIDENT
OLYMPUS

WILEY

NANO · MICRO small
www.small-journal.com

Graphene Nanobeacons with High-Affinity Pockets for Combined, Selective, and Effective Decontamination and Reagentless Detection of Heavy Metals

David Panáček, Lukáš Zdražil, Michal Langer, Veronika Šedajová, Zdeněk Baďura, Georgio Zoppellaro, Qiuyue Yang, Emily P. Nguyen, Ruslan Álvarez-Diduk, Vítězslav Hrubý, Jan Kolařík, Nikolaos Chalmpes, Athanasios B. Bourlinos, Radek Zbořil, Arben Merkoçi, Aristides Bakandritsos, and Michal Otyepka**

Access to clean water for drinking, sanitation, and irrigation is a major sustainable development goal of the United Nations. Thus, technologies for cleaning water and quality-monitoring must become widely accessible and of low-cost, while being effective, selective, sustainable, and eco-friendly. To meet this challenge, hetero-bifunctional nanographene fluorescent beacons with high-affinity pockets for heavy metals are developed, offering top-rated and selective adsorption for cadmium and lead, reaching 870 and 450 mg g^{-1}, respectively. The heterobifunctional and multidentate pockets also operate as selective gates for fluorescence signal regulation with sub-nanomolar sensitivity (0.1 and 0.2 nM for Pb^{2+} and Cd^{2+}, respectively), due to binding affinities as low as those of antigen-antibody interactions. Importantly, the acid-proof nanographenes can be fully regenerated and reused. Their broad visible-light absorption offers an additional mode for water-quality monitoring based on ultra-low cost and user-friendly reagentless paper detection with the naked-eye at a limit of detection of 1 and 10 ppb for Pb^{2+} and Cd^{2+} ions, respectively. This work shows that photoactive nanomaterials, densely-functionalized with strong, yet selective ligands for targeted contaminants, can successfully combine features such as excellent adsorption, reusability, and sensing capabilities, in a way to extend the material's applicability, its life-cycle, and value-for-money.

1. Introduction

The increasing impact on the worldwide eco-systems of anthropogenic activities (transportation, industrial, agricultural, and mining activities[1,2]) contributes substantially to the accumulation of toxic heavy metals in the earth's upper crust,[3] making the availability of high quality water for drinking and sanitation (a major sustainable development goal of the United Nations) into a growing challenge.[4] Several billions of people have limited access to clean water (with estimates approaching half of the population by 2025),[5,6] thus the development of advanced materials and technologies is pivotal for efficient remediation and user-friendly/on-site water quality-monitoring, in order to secure a sustainable, and technologically advanced civilization.

Undoubtedly, advances in the design of tailored inorganic and carbon-based materials have provided access to new and efficient nanostructures for sorption

D. Panáček, L. Zdražil, M. Langer, V. Šedajová, Z. Baďura, G. Zoppellaro, V. Hrubý, J. Kolařík, R. Zbořil, A. Bakandritsos, M. Otyepka
Regional Centre of Advanced Technologies and Materials
Czech Advanced Technology and Research Institute (CATRIN)
Palacký University Olomouc
Šlechtitelů 241/27, Olomouc 783 71, Czech Republic
E-mail: a.bakandritsos@upol.cz; michal.otyepka@upol.cz

The ORCID identification number(s) for the author(s) of this article can be found under https://doi.org/10.1002/smll.202201003.

© 2022 The Authors. Small published by Wiley-VCH GmbH. This is an open access article under the terms of the Creative Commons Attribution License, which permits use, distribution and reproduction in any medium, provided the original work is properly cited.

DOI: 10.1002/smll.202201003

D. Panáček, L. Zdražil, M. Langer, V. Šedajová, V. Hrubý
Department of Physical Chemistry
Faculty of Science
Palacký University Olomouc
17. listopadu 1192/12, Olomouc 771 46, Czech Republic

D. Panáček, Q. Yang, E. P. Nguyen, R. Álvarez-Diduk, A. Merkoçi
Catalan Institute of Nanoscience and Nanotechnology
Autonomous University of Barcelona
CSIC and BIST, Campus UAB, Bellaterra, Barcelona 08193, Spain

Z. Baďura
Department of Experimental Physics
Faculty of Science
Palacký University Olomouc
17. listopadu 1192/12, Olomouc 771 46, Czech Republic

N. Chalmpes
Department of Materials Science & Engineering
University of Ioannina
Ioannina 45110, Greece

Check for updates
16136829, 2022, 33, Downloaded from https://onlinelibrary.wiley.com/doi/10.1002/smll.202201003 by Spanish Cochrane National Provision (Ministerio de Sanidad), Wiley Online Library on [18/10/2022]. See the Terms and Conditions (https://onlinelibrary.wiley.com/terms-and-conditions) on Wiley Online Library for rules of use; OA articles are governed by the applicable Creative Commons License

technologies, the latter remaining among the most facile and effective methods for water decontamination due to their simplicity and efficiency.[7,8] However, the next generation of sorbents has to integrate the advantages of large accessible surface with chemical functionalization, acting as potent and selective ligands for targeted contaminants.[9–15] A prerequisite for the broad application of such sophisticated and costly sorbents is the integration of features of high added-value, such as sustainability (i.e., sorbent regeneration and reuse),[10,16] catalytic activity after metal adsorption,[1,12,16] or utilization of the same material for water-quality monitoring.[17–20] The combination of water decontamination and user-friendly water-quality monitoring is particularly attractive, since the two applications are highly complementary to each other, both from mechanistic and practical aspects. A potent sorbent requires a material that can attract the target analyte onto its surface with high affinity, significantly increasing locally the analyte's concentration. This may greatly impact the sensing if the sorbent simultaneously offers an analyte-dependent signal. A variety of nanomaterials such as Ag and Au NPs,[21–23] inorganic quantum dots,[24–26] graphene/carbon dots,[19,26–31] WS_2 sheets,[32] metal organic frameworks (MOFs),[17] and 2D organic frameworks[33,34] have been utilized to develop nanosensors for the detection of metal ions. Among them, tailor-coated Au-NP films have demonstrated selective, attomolar detection for methylmercury, and picomolar detection for Cd^{2+} (less selective) via changes in tunneling currents.[23] Although extremely sensitive, the use of noble metals and required methodology suggest the use of the sensor in dedicated high-end applications, where detection far below the drinking water allowance limits is required. Other sensing schemes rely on specialized (bio)molecules (DNA/aptamers,[22,28,35–39] proteins,[40] organic molecules,[41] metal ion-imprinted polymers[25]) to achieve selectivity and high binding affinity. Carbon/graphene dots may offer low limits of detection (LoDs; Table S1, Supporting Information) via simple fluorometric or electrochemical sensing, owing to their particularly small size, high surface area, and chemically rich shell, allowing for coordination with metal ions or further derivatization.[19,26,28–30] Along with their sustainability, excellent biocompatibility, and eco-friendly character,[42–44] they overall shape a very attractive ground for innovation.

However, high selectivity for the toxic metals is often an issue,[19,21,45] while the combined adsorption and sensing of target analytes is particularly challenging.[17–20] For example, a Ca^{2+}-MOF exhibited both adsorption and voltametric detection of Pb^{2+} and Cd^{2+}, with one of the highest Pb^{2+} adsorption capacities (≈522 mg g^{-1}; and 220 mg g^{-1} for Cd^{2+}) and LoD of 3.0 and 11.6 nM for Pb^{2+} and Cd^{2+}, respectively.[17] However, the MOF was unstable in the highly acidic regeneration medium and thus not reusable. Furthermore, sensing in presence of competitive cations from drinking water (such as Ca^{2+} and Mg^{2+}) might also be an issue since the material exhibited similar sensitivities for a wide variety of metal ions (with both low and high toxicities). In another case, exploiting the fluorescence, porosity, and thioether-functionalization of covalent organic frameworks (COFs), the highly selective fluorometric detection and facile removal of Hg^{2+} was achieved.[18] Nevertheless, the sorbent was unstable in water, showing better sensing in organic solvents, and despite the exceptional selectivity, the sensitivity of 120 nM was suboptimal, since the maximum allowance limits for the toxic metals in drinking water (e.g., Hg^{2+}, Pb^{2+}, Cd^{2+}) are all bellow 80 nM.[46] Furthermore, the hydrazone bonds of the COF, although covalent, are highly labile, precluding the utilization of aggressive regeneration media, required for the desorption of the adsorbed metal ions and recycling of the sorbent. Amino-functionalized carbon dots were also successfully applied for dual adsorption and sensing reaching 0.5 nM LoD for Pb^{2+}.[19] Nevertheless, the detection was based on monitoring the absorbance at extremely low wavelength (215 nm, where tap and river water composition blocks this spectral window, as shown in Figure S1, Supporting Information), restricting the application in real samples. The response was found similar to other metals (Fe^{3+} and Mn^{2+}) with much lower toxicity than Pb^{2+}, further limiting the applicability. The challenge grows enormously when such dual function should be combined with sorbent recyclability, high adsorption capacity, detection selectivity, and sensitivity in order to bring added values and high potential for applicability. Key properties to achieve this embrace structural stability, high binding affinities[10] for the target metals, and an interaction mechanism intrinsically regulating the transduction sensing signal.[40]

In order to overcome these challenges, we engineered dual functionalized graphene fluorescent nanobeacons equipped with carboxyl groups and nitrogen doping. A synthesis of the nitrogen-doped graphene derivative (NG, **Figure 1**a) was followed by oxidation and size confinement, leading to a fluorescent and carboxyl-functionalized nitrogen-doped graphene acid (NGA, Figure 1b). The NGA proved a very efficient and selective trap for Pb^{2+} and Cd^{2+} ions (Figure $1b_1$), facilitating exceptional water decontamination in presence of competing ions (Table S2, Supporting Information), both in simulated and real samples. After a hydrothermal treatment of NGA and formation of 2–3 nm NGA dots (NGA-D, Figure 1c), to further confine the lateral dimensions and boost the photoluminescence (PL) properties, the fast, reagentless, and selective detection of Pb^{2+} and Cd^{2+} was achieved via PL quenching (Figure $1c_1$). The obtained LoDs (0.1 and 0.2 nM for Pb^{2+} and Cd^{2+}, respectively) were unprecedented, surpassing the state-of-the-art schemes based on fluorometric and potentiometric methods, even many sensors using aptamers and DNA strands for sensitivity boosting,[38,47,48] (Table S1, Supporting Information). The high sensitivity of the NGA-D was ascribed to the very strong

A. B. Bourlinos
Physics Department
University of Ioannina
Ioannina 45110, Greece
R. Zbořil, A. Bakandritsos
Nanotechnology Centre
Centre of Energy and Environmental Technologies
VŠB-Technical University of Ostrava
17. listopadu 2172/15, Ostrava-Poruba 708 00, Czech Republic
A. Merkoçi
ICREA, Institució Catalana de Recerca i Estudis Avançats
Pg. Lluís Companys, 23, Barcelona 08010, Spain
M. Otyepka
IT4Innovations
VŠB-Technical University of Ostrava
17. listopadu 2172/15, Ostrava-Poruba 708 00, Czech Republic

© 2022 The Authors. Small published by Wiley-VCH GmbH

16136829, 2022, 33, Downloaded from https://onlinelibrary.wiley.com/doi/10.1002/smll.202201003 by Spanish Cochrane National Provision (Ministerio de Sanidad), Wiley Online Library on [18/10/2022]. See the Terms and Conditions (https://onlinelibrary.wiley.com/terms-and-conditions) on Wiley Online Library for rules of use; OA articles are governed by the applicable Creative Commons License

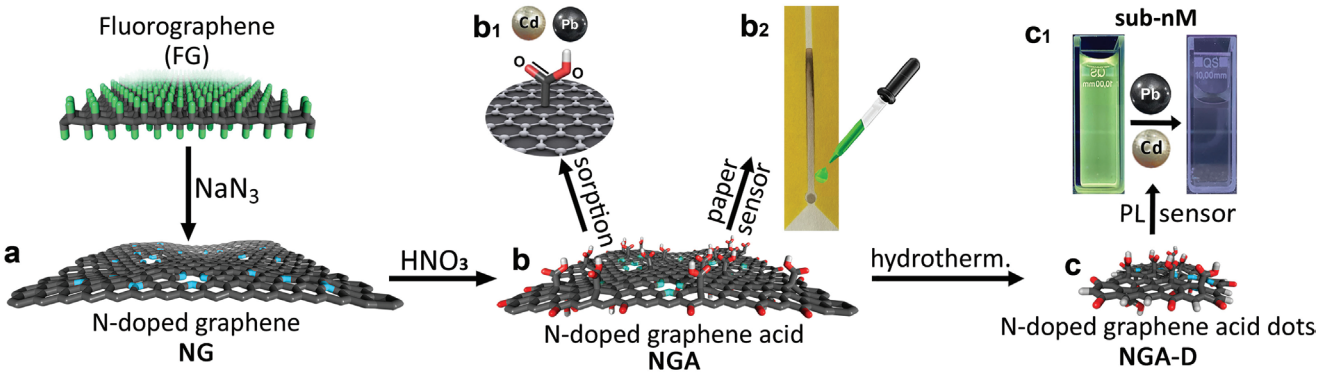

Figure 1. Synthesis and application of nitrogen-doped graphene acid. a) Synthesis of NG and b) oxidation to NGA with its respective applications; b_1) adsorption and b_2) paper detection of Pb^{2+} and Cd^{2+}. c) Synthesis of NGA-D and c_1) application of NGA-D for selective PL detection of Pb^{2+} and Cd^{2+}.

binding for Pb^{2+} and Cd^{2+} inside a multivalent coordination pocket formed by the nitrogen doped-vacancies and the carboxyl groups, with association constants in the order of antigen antibody-interactions (10^{-6}–10^{-9} L м$^{-1}$),[49] and with a direct binding mechanism involving the formation of dark complexes with the ground-state of the NGA dots. Importantly, the acid-proof structure of NGA enabled its full regeneration and reuse as sorbent, while its broad visible-light absorption offered an additional sensing mode for the two toxic metals based on reagentless detection with naked-eye on paper, offering a solution for ultra-low cost, and user-friendly water quality monitoring (Figure 1b_2).

2. Results and Discussion

NG was obtained by the reaction of fluorographene with sodium azide, as previously reported,[50] leading to extensive defluorination, and to 11.6 at% nitrogen doping, according to X-ray photoelectron spectroscopy results (XPS, **Figure 2**a,b). The deconvoluted C 1s domain of the high-resolution XPS (HR-XPS, Figure 2c) spectra showed that NG consisted mostly of sp^2 carbons (66.3 at%), C—N—C carbons (25.9 at%), and CO groups (5.2 at%, (Table S3, Supporting Information). The deconvolution of N 1s spectrum (Figure S2, Supporting Information) showed a typical three-component pattern characteristic for nitrogen doped graphene, reflecting pyridinic, pyrrolic, and graphitic nitrogen configurations (Table S4, Supporting Information).[51] Oxidation of NG with nitric acid afforded the NGA product, where the oxygen content increased from 3.0 at% to 32.7 at% and nitrogen decreased to 5.2 at%; (Figure 2a,b, Table S5, Supporting Information). According to the deconvolution of the C 1s and O 1s HR-XPS spectral regions, 15.2 at% of the total carbons corresponded to carboxylic carbons, 10.5 at% to C=O carbons, and another ≈10 at% to C—O carbons (Figure 2c,d; Tables S5 and S6, Supporting Information). NGA sheets were downsized by hydrothermal treatment into graphene dots of 2.5 nm (NGA-D product), accompanied by further oxidation, as evidenced by the increase in oxygen content (Figure 2a,b), ascribed to the oxidative cutting of the sheets. HR-XPS results showed that 25.2 at% of the carbons corresponded to carboxylic groups, and 11.7 at% to C=O groups, while all C—OH groups were transformed to carboxyls (Figure 2c,d; Tables S5 and S6, Supporting Information). The nitrogen content of NGA-D dropped to 4.9 at% (Figure 2b; Tables S4 and S6, Supporting Information).

Fourier-transformed infrared spectroscopy (FT-IR, Figure 2e) showed that the NG spectrum was dominated by two bands at 1560 cm^{-1}, and between 1000 and 1210 cm^{-1}, both corresponding to skeletal vibrations of the sp^2 aromatic carbon network and to aromatic rings.[52,53] The feature at 1395 cm^{-1} indicated heteroatom substitution in aromatic rings, for example, to pyridinic ring vibrations.[53,54] In agreement with XPS, the spectra of NGA and NGA-D revealed the characteristic stretching band of the carbonyl group at 1720 cm^{-1} (Figure 2e) from the carboxyls. The broad band at 1230 cm^{-1} changed its pattern in comparison to NG, comprising now also the C—O stretching modes from the carboxylic groups.[55] Ionization of the carboxylic groups to carboxylates gave rise to additional vibrations at 1600 cm^{-1} and at 1420/1350 cm^{-1}, ascribed to $-CO_2^-$ asymmetric and symmetric stretching, respectively.[56] The band in NGA at 1140 cm^{-1} reflects the presence of C—OH groups, which significantly decreased upon further oxidation in NGA-D, corroborating the XPS results. The aromatic ring vibrations at 1560 cm^{-1} were present in both NGA and NGA-D, in agreement to the sp^2 carbon components observed in XPS. The new band at 1650 cm^{-1} in NGA-D was attributed to a small amount of organic nitrate groups (R–O–NO_2 Figure S3 and Table S4, Supporting Information), which typically have a very strong asymmetric band in this region.[57] Further details supporting the FT-IR analysis are provided in the Supporting Information (Figure S3, Supporting Information).

The morphology and microstructure of NG, NGA, and NGA-D were analyzed by transmission electron microscopy (TEM), showing that NG comprised few-layered graphene flakes with size around 600 nm (**Figure 3**a). The NGA flakes were smaller, ≈50 nm, due to the oxidative cutting from the action of concentrated nitric acid, showing high proclivity to interact with each other (Figure 3b). Elemental mapping of NGA confirmed the homogeneous coverage of the flakes with nitrogen and oxygen (Figure 3c–f), coinciding with the spatial distribution of carbon. After hydrothermal treatment at 90 °C, graphene dots of very small size in the range of 2–3 nm were formed (NGA-D), with a lattice spacing of 0.21 nm corresponding to that of graphene {1100} lattice fringes[28] (Figure 3h, Figure S4a–d, Supporting Information). After measurement of lattice spacings from more

© 2022 The Authors. Small published by Wiley-VCH GmbH

16136829, 2022, 33, Downloaded from https://onlinelibrary.wiley.com/doi/10.1002/smll.202201003 by Spanish Cochrane National Provision (Ministerio de Sanidad), Wiley Online Library on [18/10/2022]. See the Terms and Conditions (https://onlinelibrary.wiley.com/terms-and-conditions) on Wiley Online Library for rules of use; OA articles are governed by the applicable Creative Commons License

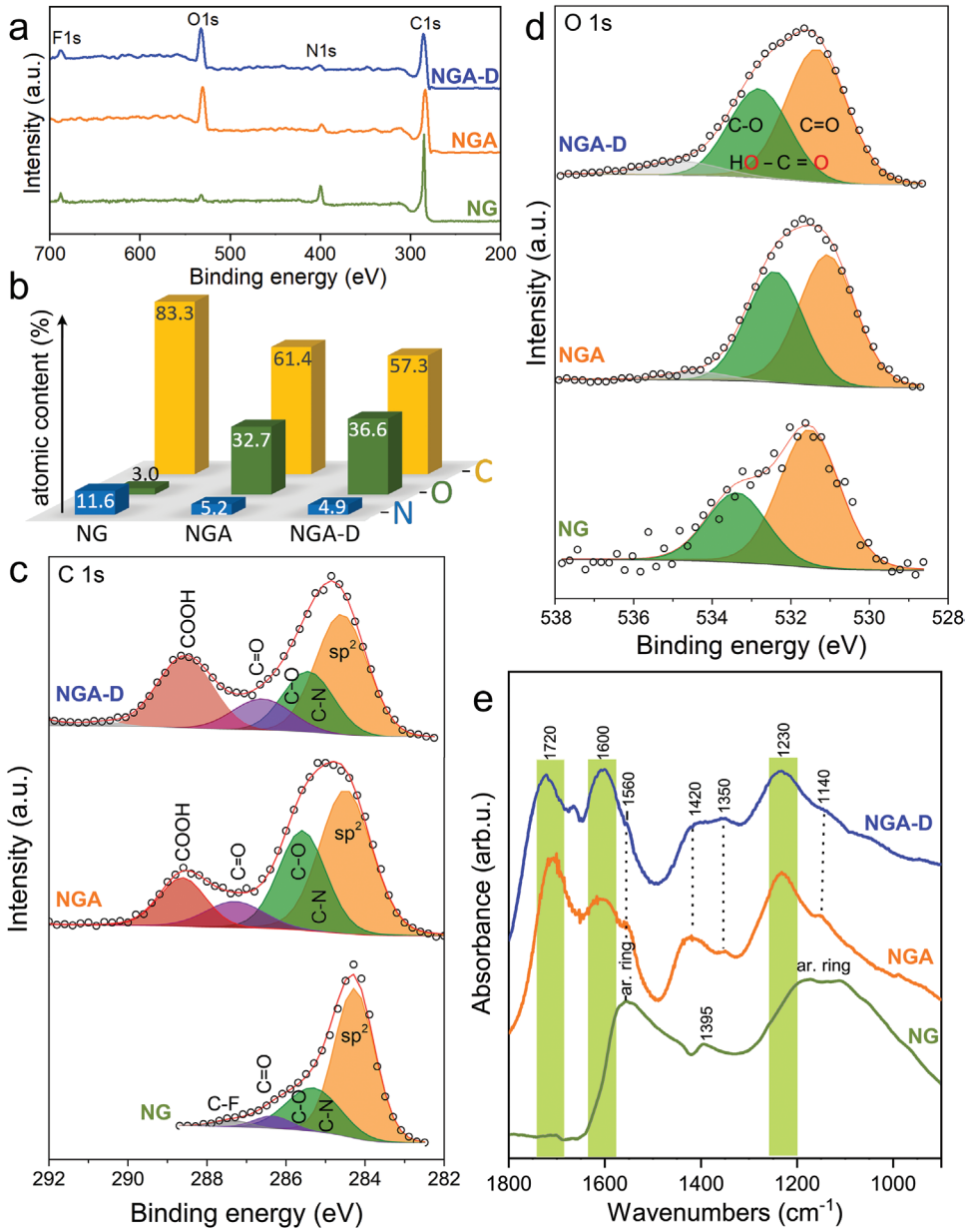

Figure 2. a) XPS survey spectra, b) Atomic contents of the nitrogen doped-graphene (NG), after its treatment with nitric acid (NGA) and after hydrothermal treatment (NGA-D), c) HR-XPS C 1s, d) HR-XPS O 1s and e) FT-IR spectra of NG, NGA, and NGA-D.

dots (Figure S4c,d, Supporting Information), only these fringes were observed, confirming the dominant presence of single or few-layered graphene dots sitting flat on the grid, rather than carbon dots, which are multilayered with interlayer spacing of ≈3.4 nm. The abundance of single-layered graphene dots was further confirmed from the selected area diffraction from many dots, showing the {1100} diffraction peak much brighter than the {2110}[58,59] (Figure S4b, Supporting Information). Atomic force microscopy (AFM, Figure 3i) showed an average thickness of 3 nm, corresponding to single-layer sheets, considering that unfunctionalized single layer graphene shows AFM thickness up to 2.6 nm.[59]

PL measurements at room temperature of NG, NGA, and NGA-D dispersed in water did not show any PL for NG, but after oxidation NGA exhibited a PL maximum at 523 nm under 470 nm excitation (**Figure 4**a). The appearance of PL can be ascribed to quantum confinement effects due to the development of small sp^2 islands isolated by the sp^3 carbons bonded to the oxygen functionalities, overall forming the PL-active surface states. The thermal treatment of NGA resulted to PL enhancement in the NGA-D product, keeping the same photophysical characteristics (Figure 4a), which could be thus attributed to the significant reduction of the lateral dimensions of the NGA sheets in the form of discrete dots, increasing further the content in quantum-confined areas.[60–62] The increased PL intensity could be also ascribed to the improved quality of the dispersion in the NGA-D product in comparison to the NGA system, since interparticle interactions can cause PL

© 2022 The Authors. Small published by Wiley-VCH GmbH

16136829, 2022, 33, Downloaded from https://onlinelibrary.wiley.com/doi/10.1002/smll.202201003 by Spanish Cochrane National Provision (Ministerio de Sanidad), Wiley Online Library on [18/10/2022]. See the Terms and Conditions (https://onlinelibrary.wiley.com/terms-and-conditions) on Wiley Online Library for rules of use; OA articles are governed by the applicable Creative Commons License

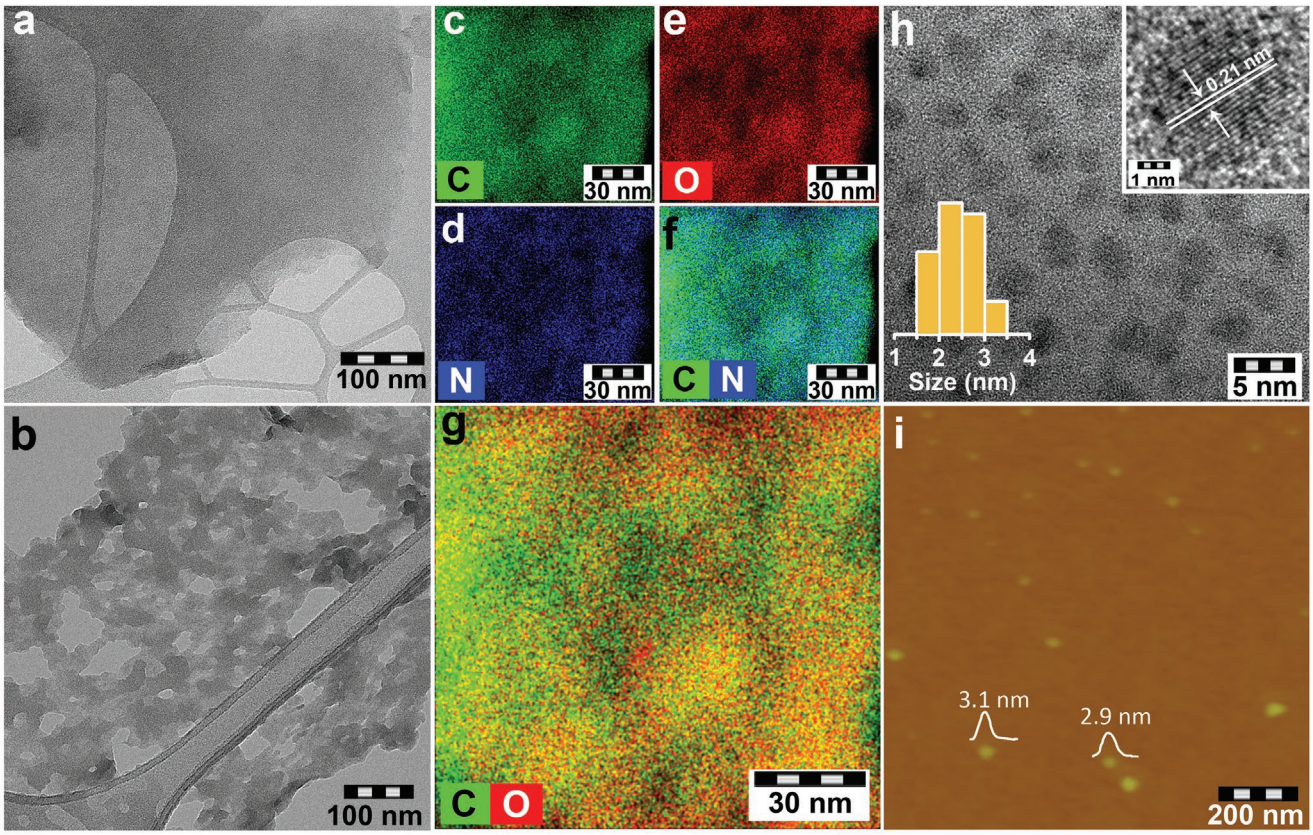

Figure 3. TEM images of a) NG and b) NGA. EDS chemical mapping of c) carbon, d) nitrogen, and e) oxygen and combined chemical mapping of f) carbon plus nitrogen and g) carbon plus oxygen of NGA. h) HR-TEM image of NGA-D, with insets presenting resolved crystalline lattice (top right) and size distribution of NGA-D (bottom left). i) AFM image of NGA-D with height profiles along the indicated white line.

quenching.[63] The excitation-emission map of NGA-D showed excitation-independent emission (Figure 4b), suggesting that PL originates from dots with very similar band-gap states, due to their monodispersity.[61,63] Along with the small Stokes-shift of ≈50 nm (Figure 4c), these observations suggest the absence of interlayer interactions, which usually lead to formation of excimers and energy-transfer (responsible for the large Stokes-shift and excitation-dependent PL, respectively) in carbon dots.[64] The absorption spectra of the products (Figure 4c, at 0.5 mg mL^{-1}) at the long wavelengths (i.e., above 700 nm, where light scattering phenomena mainly dominate) showed decreasing absorbance going from NG to NGA and to NGA-D, verifying that the flake size also decreases with the same order from NG to NGA and to NGA-D. The absorption spectrum of NGA-D showed a perturbation between 400 and 500 nm, with a maximum at 460 nm, as verified by the derivative curve (Figure 4c), coinciding well with the excitation maximum of 467 ± 2 nm. The band-gap value of 2.8 eV (i.e., 440 nm) for the NGA-D, as calculated from the Tauc plot (Figure S5, Supporting Information), was also found in agreement with the spectral features. The PL emission peak of NGA-D under the excitation of 467 nm was centered at 527 nm (FWHM of 119 nm) with a PL lifetime of 1.1 ns, as obtained from fitting the PL decay by a stretched-exponential function (Figure 4d).

The carboxyl groups are very strong metal-coordinating ligands, and exhibit particularly high adsorption capacities for Cd^{2+} and Pb^{2+}.[10,12,65] Indeed, NGA showed a substantially enhanced adsorption capacity, reaching 872 mg g^{-1} for Pb^{2+} (at 100 ppm Pb^{2+} feed, pH = 3.5), while NG reached 170 mg g^{-1} (Table S2 Supporting Information), confirming the key role of carboxyl groups in NGA. As a result, NGA outperformed state-of-the-art sorbents (**Figure 5**a). The same trend was observed for the case of Cd^{2+}, with NG reaching a capacity of 97 mg g^{-1} which was only a fraction of NGA's capacity of 448 mg g^{-1} (at 100 ppm Cd^{2+} feed, pH = 3.5), surpassing the capacity of most of the recently reported sorbents (Figure 5b). The sorption isotherms showed higher affinity for Pb^{2+} than for Cd^{2+}, as indicated from the Langmuir and Freundlich constants, and from magnitudes of mean free sorption energy derived from data fitting analysis (Figure S6, Supporting Information). The higher affinity for Pb^{2+} was also evident from the adsorption rate that was higher for Pb^{2+} than for Cd^{2+} based on the kinetic monitoring of the process analyzed by fitting the data to three different kinetic models (Figure S7, Supporting information). A highly detailed information about the analysis of the adsorption processes is in the Supporting information. The adsorption capacities at higher pH values were further improved, but the results are affected by metal-ion hydrolysis (in more detail in the Supporting information). The adsorption properties of NGA were further tested in presence of competing ions that are found in mineral water (Ca^{2+}, Mg^{2+}, Na^{+}, K^{+}; the concentrations are available in the Supporting Information) and

© 2022 The Authors. Small published by Wiley-VCH GmbH

16136829, 2022, 33, Downloaded from https://onlinelibrary.wiley.com/doi/10.1002/smll.202201003 by Spanish Cochrane National Provision (Ministerio de Sanidad), Wiley Online Library on [18/10/2022]. See the Terms and Conditions (https://onlinelibrary.wiley.com/terms-and-conditions) on Wiley Online Library for rules of use; OA articles are governed by the applicable Creative Commons License

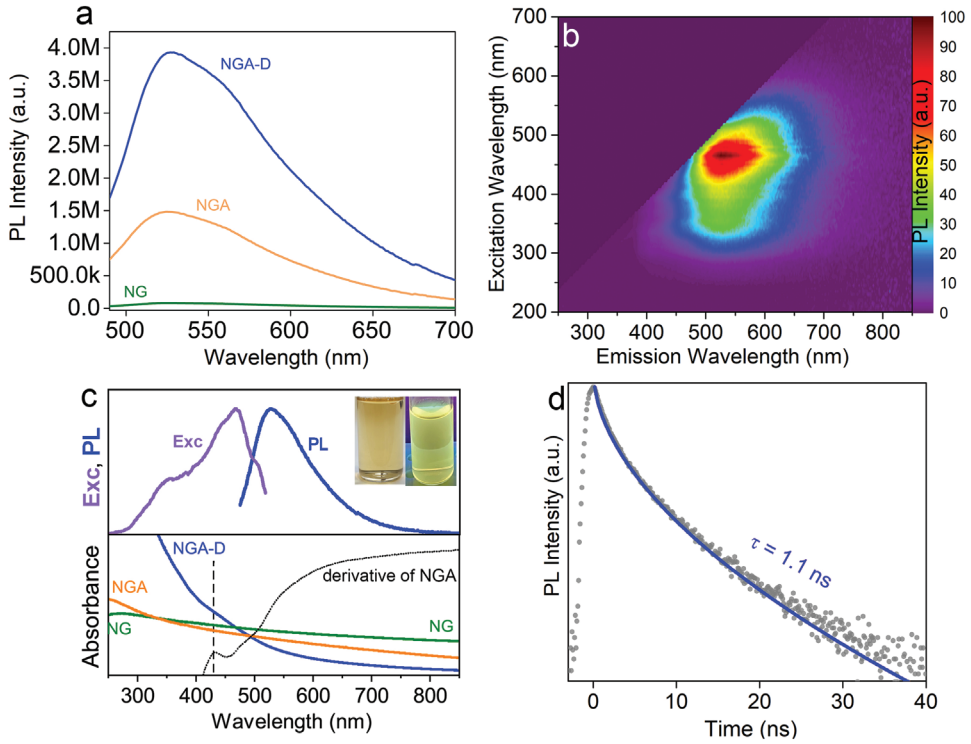

Figure 4. a) Comparison of PL spectra of NG, NGA, and NGA-D (λ_{ex} = 470 nm, 0.5 mg mL^{-1}). b) Excitation-emission color map of NGA-D. c) UV–vis absorption spectra of NG, NGA, and NGA-D (with its derivative), along with the excitation (λ_{ex} = 467 nm) and PL (λ_{em} = 527 nm) spectra of NGA-D. The inset in the PL panel shows the aqueous NGA-D dispersion under ambient light and under 365 nm irradiation. d) Time-resolved PL decay (λ_{em} = 527 nm) with corresponding stretched-exponential fit (blue line) for derivation of the PL lifetime.

in river water (Figure 5c). The results highlighted a very low decrease of the adsorption capabilities (15% and 20% decrease for Pb^{2+} and Cd^{2+}, respectively, in river water), suggesting the high selectivity of NGA toward the heavy metal ions. To fully validate the witnessed high selectivity, adsorption experiments in presence of Pb^{2+} and Ca^{2+} (both at 100 ppm feed, pH = 3.5) were carried out, which showed only 10% decrease in the Pb^{2+} adsorption (from 872 to 780 mg g^{-1}, Figure 5c). According to the principle of hard and soft acids and bases, the selectivity can be explained as H_2O molecules are considered as "hard base" ligands, therefore coordinating and keeping in solution the very "hard acid" metal ions of Mg^{2+} and Ca^{2+} (which is also reflected by the high hydration energy of these cations), rather than the intermediate "soft acid" cations of Cd^{2+} and Pb^{2+}, which coordinate better with the carboxyl groups.[66] NGA appears to have similar adsorption capacity for Pb^{2+} and Cd^{2+} in terms of moles (4.2 and 4 mmol g^{-1}, respectively). Nevertheless, competing adsorption experiments with simultaneous presence of Pb^{2+} and Cd^{2+} at 100 ppm feed for both meal ions, showed that Pb^{2+} adsorption dropped only by 7% and by 40% for Cd^{2+} in comparison to the single metal ion experiments, suggesting the higher affinity for Pb^{2+} than for Cd^{2+}, as confirmed from the Langmuir constants after fitting the sorption isotherms (Figure S6, Supporting Information).

To render NGA applicable and competitive against the low-cost active carbons, complementary properties are required, such as reusability. Owing to its covalently bound, non-labile metal-coordination functionalities, NGA could be treated under harsh acidic conditions (2% v/v HCl), without affecting its structure and thus its adsorption properties. Therefore, the NGA, collected after the adsorption experiments, was regenerated by acidic washing to desorb the metals, treated with 1% w/v NaOH to establish the carboxylate form, washed, dried, and then reused for the next adsorption experiments. Indeed, NGA retained its adsorption capacities for both Pb^{2+} and Cd^{2+} for at least six regeneration cycles at levels higher than 90% (Figure S8, Supporting Information), eliminating the relatively increased costs of the sorbent.

Motivated by these adsorption results, which suggested that NGA can selectively concentrate the Pb^{2+} and Cd^{2+} cations on its surface, we identified that its PL signal was quenched upon interaction with Pb^{2+} and Cd^{2+}, suggesting its applicability as a heavy-metal sensor. NGA clearly showed quenching in presence of 1 ppb (≈5 nM) of Pb^{2+} (Figure S9a, Supporting Information). This property was boosted significantly in NGA-D, which has very similar composition, but it is more finely dispersed, has stronger PL, and smaller size, predisposing it as a better candidate for the application, showing quenching even at 0.05 ppb (≈0.25 nM) of Pb^{2+} (Figure S9b, Supporting Information). The quenching was also highly selective (Figure 5d), even in natural mineral water and tap water samples, which contained much higher concentrations of other divalent metals (Figure 5d). The LoDs (at a signal-to-noise ratio of 3) were as low as 0.1 nM for Pb^{2+} and 0.2 nM for Cd^{2+}, as determined from PL intensity versus metal concentration curves, (Figure S10, Supporting Information), outperforming previously reported systems (**Figure 6**e,f and Table S1, Supporting Information), including electroluminescent graphene dots (LoD(Cd^{2+}) = 13 nM[67]) and DNA based-sensors

© 2022 The Authors. Small published by Wiley-VCH GmbH

16136829, 2022, 33, Downloaded from https://onlinelibrary.wiley.com/doi/10.1002/smll.202201003 by Spanish Cochrane National Provision (Ministerio de Sanidad), Wiley Online Library on [18/10/2022]. See the Terms and Conditions (https://onlinelibrary.wiley.com/terms-and-conditions) on Wiley Online Library for rules of use; OA articles are governed by the applicable Creative Commons License

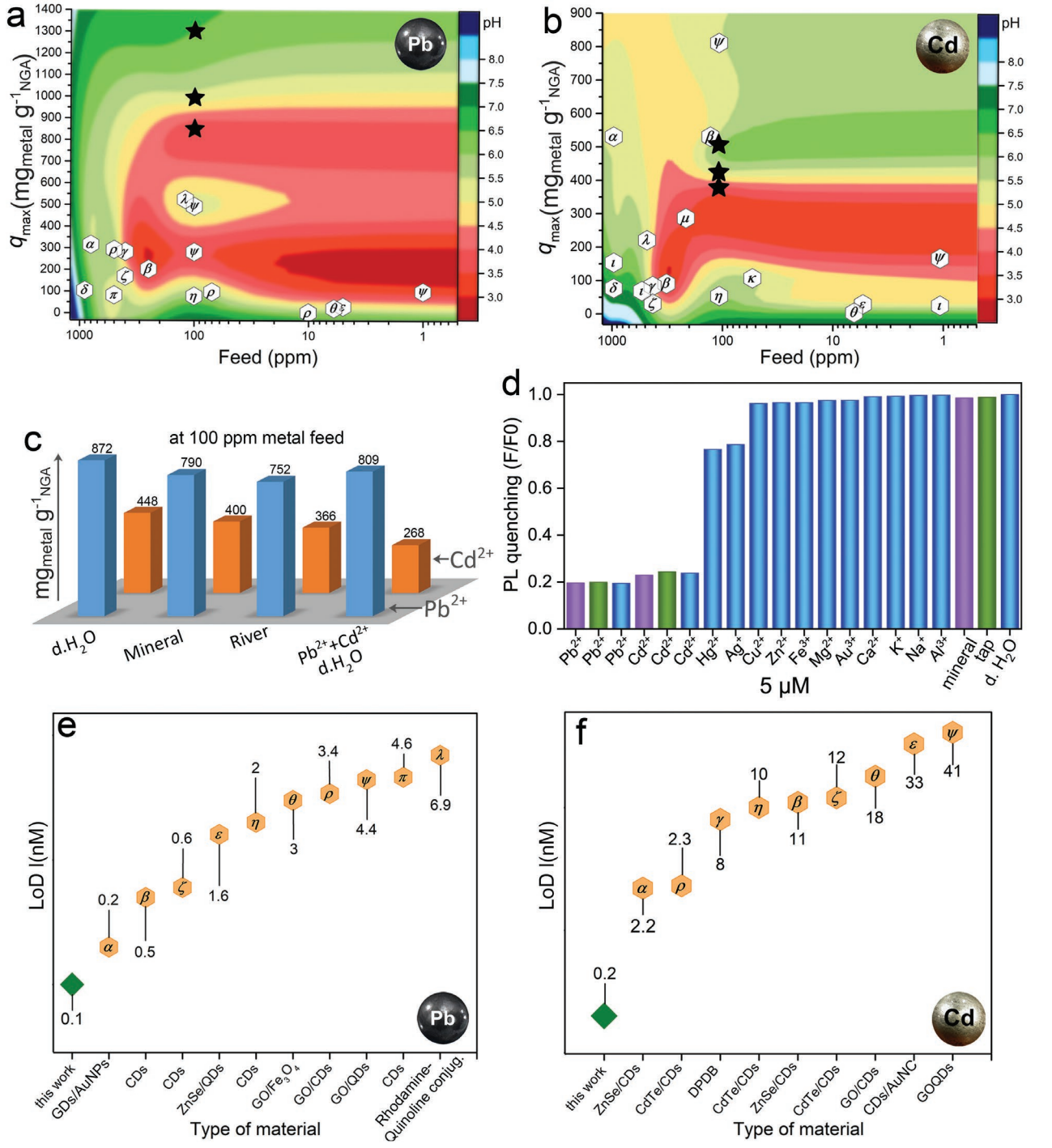

Figure 5. a,b) Comparative graph showing the adsorption capacities (q_{max}) for Pb^{2+} and Cd^{2+} for NGA (star symbols) and for previously reported sorbents at various metal feeds and pH values: (α) MOF-808(Zr) modified with EDTA,[10] (β) GO,[68] (γ) GO/polymer hydrogel,[69] (δ) carbon nanotube sheets,[70] (ε) GO, amino-modified and decorated with Fe_3O_4 nanoparticles,[71] (ζ) copolymer modified Fe_3O_4 nanoparticles,[72] (η) silica gel modified with nitrilotriacetic acid,[73] (θ) GO decorated by iron-based nanoparticles,[74] (ι) GO,[75] (κ) GO,[76] (λ) 2D Ca^{2+}-MOF,[17] (μ) FJI-H9 MOF modified with amino groups,[77] (π) α-FeOOH,[78] (ρ) LDH modified with MoS_4^{2-},[79] (ψ) graphene acid.[12] c) Adsorption capacities at pH = 3.5 for Pb^{2+} and Cd^{2+} in distilled, mineral, and river water, as well in combined Pb^{2+} and Cd^{2+} solutions in distilled water. In all experiments, the initial metal feed was 100 ppm. d) Comparison of fluorescence quenching of NGA-D induced by Pb^{2+}, Cd^{2+}, and other metal ions at 5 µM concentration in ultra-pure water (blue), tap water (green), and mineral water (purple). e) Comparative graph showing the LoD values for Pb^{2+} for NGA-D and from the state-of-the-art material sensors. (α) GQDs modified with AuNPs,[21] (β) CDs,[19] (ζ) CDs,[29] (ε) ZnSe QDs,[25] (η) CDs,[45] (θ) GO dots modified with Fe_3O_4,[80] (ρ) GO combined with CDs,[81] (ψ) GO combined with QDs,[38] (π) CDs,[30] (λ) Rhodamine–Quinoline Conjugates.[82] f) Comparative graph showing the limit of detection for Cd^{2+} for NGA-D and for top-rated results from literature. (α) ZnSe/CDs,[25] (ρ) CdTe QDs,[26] (γ) DPDB ligand,[83] (η) CdTe QDs,[84] (β) ZnSe/CdS,[24] (ζ) CdTe QDs,[85] (θ) GO combined with CDs,[86] (ε) CDs modified with gold nanoclusters[87] and (ψ) GOQD.[38]

© 2022 The Authors. Small published by Wiley-VCH GmbH

16136829, 2022, 33, Downloaded from https://onlinelibrary.wiley.com/doi/10.1002/smll.202201003 by Spanish Cochrane National Provision (Ministerio de Sanidad), Wiley Online Library on [18/10/2022]. See the Terms and Conditions (https://onlinelibrary.wiley.com/terms-and-conditions) on Wiley Online Library for rules of use; OA articles are governed by the applicable Creative Commons License

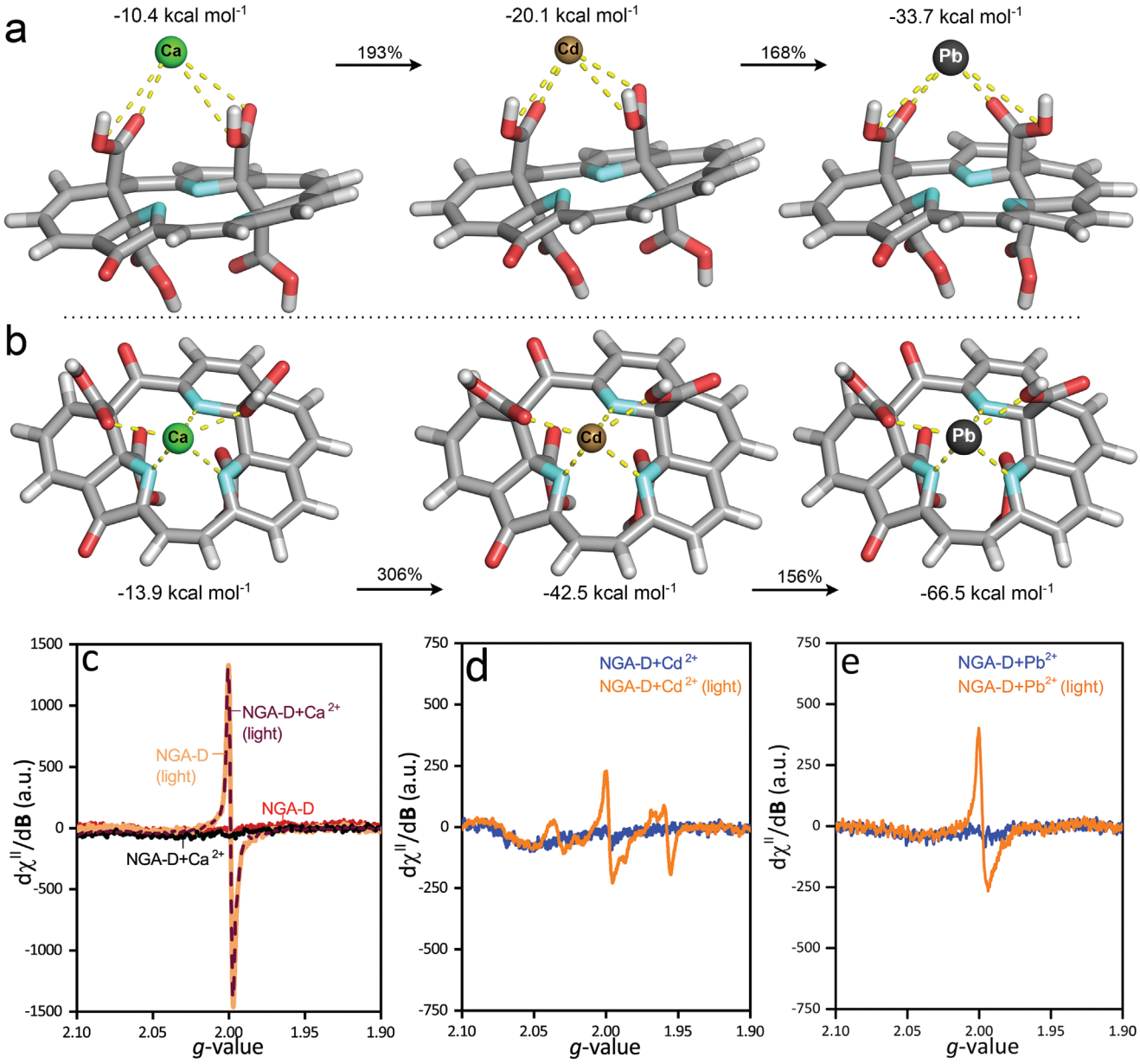

Figure 6. Interaction of three divalent ions (Ca^{2+}, Cd^{2+}, and Pb^{2+}) with molecular models of NGA-D, displaying two energetically favorable binding positions comprising a) carboxyl groups only and b) carboxyl groups plus nitrogen atoms, along with their corresponding binding energies (Figures S13 and S14, Supporting Information for further details). X-band CW-EPR and CW-LEPR spectra of NGA-D dispersed in H_2O and measured in frozen matrix ($T = 80$ K) of c) pure NGA-D recorded under dark conditions (red line) and under UV irradiation (orange line) and NGA-D with adsorbed Ca^{2+} cations recorded under dark conditions (black line) and under UV irradiation (purple dashed line). d) NGA-D with adsorbed Cd^{2+} cations recorded under dark conditions (blue line) and under UV irradiation (orange line). e) NGA-D with adsorbed Pb^{2+} cations recorded under dark conditions (blue line) and under UV irradiation (orange line).

(LoD(Cd^{2+}) = 10 nM;[47] LoD(Pb^{2+}) = 0.3[48] or 4.4 nM[38]). In some cases, low LoD values have been reported (e.g., 0.2 and 2.2 nM for Pb^{2+} and Cd^{2+}, respectively[21,25]) via the PL turn-on of gold nanoparticles released from the graphene surface upon interaction with Pb^{2+}. Apart from the use of noble metals, the Pb^{2+} sensor showed similar selectivity for the much less toxic Mn^{2+} ions, limiting its applicability.[21] The sensor with 2.2 nM LoD for Cd^{2+} relied on the coating of the ZnSe dots with metal cation-imprinted polymers, and, apart from the PL spectrometer, a sophisticated microfluidic chip was required for analysis and detection.[25] Despite this, the LoD values were significantly inferior to the NGA-D sensor. Finally, such materials are not suitable for heavy metal-sorption and water decontamination, unlike NGA-D, whose precursor (NGA) exhibits top-rated sorption for the two heavy metal ions. Due to the high selectivity, NGA-D sensing ability was further challenged in mineral water and tap water, showing the same LoD values as in ultrapure water (Figure S11, Supporting Information), which were found well below the drinking water European concentration limits of 72 nM (15 ppb) and 44 nM (5 ppb) for Pb^{2+} and Cd^{2+}, respectively,[46]

© 2022 The Authors. Small published by Wiley-VCH GmbH

16136829, 2022, 33, Downloaded from https://onlinelibrary.wiley.com/doi/10.1002/smll.202201003 by Spanish Cochrane National Provision (Ministerio de Sanidad), Wiley Online Library on [18/10/2022]. See the Terms and Conditions (https://onlinelibrary.wiley.com/terms-and-conditions) on Wiley Online Library for rules of use; OA articles are governed by the applicable Creative Commons License

rendering NGA-D a very effective material for practical sensing of toxic heavy metals, not affected by other metals which are less toxic and with higher drinking water limits.

The high selectivity and PL sensitivity of the NGA-D in presence of Pb^{2+} and Cd^{2+} ions should be related to the highly specific electronic interactions rather than to the non-specific aggregation-induced quenching due to electrostatic interactions, as implied by the absence of PL emission peak shift.[33] Since aggregation is a slow process, the previous statement was also clearly demonstrated by the instant quenching of PL after addition of 1 or 10 μm of Pb^{2+} or Cd^{2+} (Figure S12a, Supporting Information). Only after 1 h, and after addition of 10 μm of Pb^{2+} or Cd^{2+} there is evidence of aggregation (Figure S12b, Supporting Information). Interestingly, the addition of Ca^{2+} did not cause PL quenching (Figure S12a, Supporting Information) or aggregation (Figure S12b, Supporting Information, despite it is also a divalent cation), even at 100 μm, verifying the previous results regarding the PL sensitivity and selectivity of NGA-D. Density functional theory (DFT) calculations further corroborated the results from the adsorption experiments and from the above observations. Models were constructed to correspond to the XPS composition of NGA and NGA-D and the spatial proximity of the carboxyl groups stemmed also from the actual experimental XPS data (Table S5, Supporting Information), showing a ratio of sp^2/COOH of 3 and 1.6 for NGA and NGA-D, respectively, suggesting the presence of one carboxyl group in almost every C6 ring. Two binding modes of metal cations at two different binding sites were analyzed in detail; one with carboxylic groups only and the other one with both carboxylic groups and nitrogen-doped vacancies (Figure 6a,b), which were energetically most favorable. In both cases, Ca^{2+} had significantly lower binding affinities, as indicated by the calculated binding energies which showed 2- or 3-fold stronger binding for Cd^{2+}, and Pb^{2+} showed ≈1.5-fold stronger binding even than Cd^{2+}. The 1.5-fold stronger binding was in good agreement with the experimentally determined higher association constant for Pb^{2+} than for Cd^{2+} ($\log K_L(Pb^{2+})/\log K_L(Cd^{2+}) = 4.4/3.4 = 1.3$), as obtained from the Langmuir isotherms (Figure S6, Supporting Information). The same trends were observed even when all four carboxylic groups were deprotonated (Figure S13, Supporting Information). The metal ion binding was dominated by electrostatic interaction and contribution from O and N moieties electron donation to vacant metal ions orbitals; the N-doped vacancies contributed more significantly, as evidenced by the natural bond orbital analysis (Figures S14,S15 and Table S7, Supporting Information). The key role of the N-doped vacancies in the coordination of the metal ions was also suggested by the analysis of the second-order perturbation estimates of donor-acceptor interactions, showing stronger donation to the vacant orbitals of the metal ions than the carboxylic oxygens (Figures S14,S15 and Table S7, Supporting Information). Overall, NGA and NGA-D exhibit two types of binding sites, with the minority, but stronger ones, represented by carboxylic groups plus N-doped vacancies (since nitrogen amounts to 5 at%), operating at low metal concentrations (i.e., at sub- and few-nM in the case of sensing), and carboxylic groups operating after the saturation of the former, that is, at metal cation concentrations of several μm, which is the case of the initial part of the sorption isotherms.

To shed more light on the nature of the interactions, we probed the PL decay curves with and without metals and analyzed the PL quenching results with the Stern–Volmer plots of F0/F versus metal concentration using the functions based on bimolecular theory. The derived Stern–Volmer-constants (K_{SV}) were 0.046 nM^{-1} (4.6×10^7 M^{-1}) and 0.022 nM^{-1} (2.2×10^7 M^{-1}) for Pb^{2+} and Cd^{2+}, respectively (Figure S16, Supporting Information), being in the order of antigen antibody-interactions (0.058 nM^{-1}[88] or 10^6–10^9 M^{-1}[40,49]). Indeed, such K_{SV} constants are two or three orders of magnitude larger than other CDs sensors,[45,82,86] but also than other potent sensors based on fluorescent MOFs,[33,89,90] all ranging between 3×10^4 and 4×10^5 M^{-1}. The rate constants from the Stern–Volmer plots (3.5×10^{16} M^{-1} s^{-1} and 1.7×10^{16} M^{-1} s^{-1} for Pb^{2+} and Cd^{2+}, respectively) exceeded by far the kinetics of a purely diffusion-controlled process (≈10^{10} M^{-1} s^{-1}),[90] and the PL lifetimes remained unchanged (Figure S16, Supporting Information) with or without the addition of metals, clearly indicating a static quenching mechanism. The static quenching mechanism suggests the strong and direct interaction of the metals with the ground state of NGA-D,[91] forming dark complexes after bonding between the valence band of the dots with the empty orbitals of Pb^{2+} and Cd^{2+} ions, verifying experimentally the theoretical results. The higher binding constants obtained from the PL quenching results (Figure S17, Supporting Information, 4.5×10^8 M^{-1} and 3.4×10^7 M^{-1} for Pb^{2+} and Cd^{2+}, respectively) than from the sorption isotherms (Figure S6, Supporting Information), reflected very well the theoretically obtained twofold more negative binding energies between the carboxyl-only and nitrogen-carboxyl complexes (Figure 6a,b), since the ratio of their logarithms was also equal to two ($\log K_b(Pb^{2+})/\log K_L(Pb^{2+}) = 8.7/4.4 = 1.98$, and $\log K_b(Cd^{2+})/\log K_L(Cd^{2+}) = 7.5/3.4 = 2.20$), highlighting the key role of the heterobifunctional and multivalent nitrogen-carboxyl binding sites at low metal concentrations.

The photophysics of NGA-D with Pb^{2+} or Cd^{2+}, was further studied by probing the spin-active electronic transitions with continuous wave electron paramagnetic resonance spectroscopy (CW-EPR) with and without in situ light irradiation. NGA-D was found EPR inactive under dark conditions, thus not containing free radical sites (Figure 6c). Upon irradiation, photoexcited spin-active species were clearly formed, as witnessed in the appearance of the strong EPR resonance line at $g = 1.999$ (Figure 6c, NGA-D (light)). Therefore, during the photoexcitation process, part of the excited electrons undergo intersystem crossing, forming either triplet excimers or spatially separated polarons. Due to the witnessed shape of the photogenerated paramagnetic resonance signal, we suggest that the formation upon photoexcitation of polaron pairs is preferred compared to the possible formation of excimer triplet states. Furthermore, excimer formation and relaxation (a common PL relaxation mechanism in carbon dots) is usually accompanied by a large Stokes-shift, which is not observed in NGA-D.[64] These e^-/h^+ species are thought to remain mostly localized on defect sites close to the carboxyl groups with small contribution from nitrogen sites (Figures 6a,b), because they do not exhibit, besides signal broadening, well defined hyperfine splitting in the resonance line that arises from strong coupling of the electronic spin moment with nitrogen nuclear spins (^{14}N, $I = 1$).

© 2022 The Authors. Small published by Wiley-VCH GmbH

16136829, 2022, 33, Downloaded from https://onlinelibrary.wiley.com/doi/10.1002/smll.202201003 by Spanish Cochrane National Provision (Ministerio de Sanidad), Wiley Online Library on [18/10/2022]. See the Terms and Conditions (https://onlinelibrary.wiley.com/terms-and-conditions) on Wiley Online Library for rules of use; OA articles are governed by the applicable Creative Commons License

The entrapment of Cd^{2+} and Pb^{2+}cations (1 μM) in NGA-D leads to a significant drop in the light-induced EPR signal intensity (Figure 6d,e). Therefore, coordination of both metals onto NGA-D leads to significant electronic perturbations of the e^-/h^+ photoexcited states compared to the neat material. In particular, through computer simulation of the experimental EPR resonance line, using second order perturbation theory, we found that during the photoexcitation in presence of Cd^{2+}, two sets of hole species are formed, which express axial to weakly rhombic anisotropy ((i)g_x = 2.040, $g_{y,z}$ = 1.960 and (ii) g_x = 2.003, g_y = 1.990, g_z = 1.980), while the resonance signal associated to the e^- sites remains fully isotropic ($g_{x,y,z}$ = 1.990) (Figure S18, Supporting Information). Adsorption of Pb^{2+} cations onto NGA-D also impacted the electronic fingerprint of the photogenerated e^-/h^+ species (Figure 6e), but to less extend than that expressed by coordination of Cd^{2+}. In addition to the decreased intensity of the EPR resonance signal during irradiation, the anisotropic nature of the electron spin moment tensor associated to the hole species (at lower extent than for Cd^{2+}) resulted in an asymmetric broadening of the EPR signal centered at g = 1.990, clearly seen in the high field region (Figure 6e, NGA-D+Pb^{2+}(light)). Such different behavior of the photogenerated polaron pairs in Cd^{2+} and Pb^{2+} can be interpreted in terms of their different ability to significantly modulate, upon coordination, the spatial distribution of the photoexcited spin charges on NGA-D, by perturbation of the system electric field gradient (EFG).[92] The EFG gradient is linked to $-\nabla\Phi(r)$, where $\Phi(r)$ represents the electrostatic potential present in an atom or molecule at point r caused by the distribution of charges (electrons, nuclei); hence, significant perturbation of $\Phi(r)$ on NGA-D upon metal coordination arises, as a result, of their different degrees of charge transfer, leaving a more positively charged coordinated Cd^{2+} cation (1.85 natural charge) compared to Pb^{2+} (1.70 Natural charge, see natural electron configurations in Figures S13 and S14, Supporting Information). This effect, in turn, impacts the observed variance in the h^+ electron spin moment and the vector spin anisotropy.[92] Overall, the finding that the metal ions have an impact only on the generated holes provides another proof about their interaction with the valence band of the NGA-D. Importantly, the addition of Ca^{2+} at the same concentration (1 μM) did not induce any changes, confirming the absence of interactions (Figure 6c), in accordance with the previous theoretical and experimental results.

To meet the demands for on-site, user-friendly sensing, without the need of any electronic device, allowing for very low cost and point-of-interest sensors, we developed a paper-based lateral flow sensor by leveraging the black color of NGA, along with its selective interactions to Pb^{2+} and Cd^{2+} interactions. The selected material was common chromatography nitrocellulose paper, whereby the lateral flow of NGA was guided alongside the hydrophilic channels formed by wax-printing. The resulting chromatogram was affected by the concentration of Pb^{2+} and Cd^{2+} ions (**Figure 7**), due to the strong interactions between NGA's functional groups and the heavy metal ions. This simple and fast method (requiring just 30 min for chromatogram evolution, Supporting Information, Experimental part) provides selective and quantitative information with LoDs of 0.5 and 9 μM for Pb^{2+} and Cd^{2+}, respectively (Figure 7a,b). This method of detection is even feasible for different ambient temperatures, ranging from 5 to 35 °C, allowing use in locations where temperatures are low or too high (Figure S19, Supporting Information). Considerably lower detection limits of 5 nM for Pb^{2+} and 88 nM for Cd^{2+} could be achieved after simple evaporation of the testing sample (Figure 7e,f), which are below or very close to the allowed concentrations in drinking water of 72 nM (15 ppb) and 44 nM (5 ppb) for Pb^{2+} and Cd^{2+}, respectively.[46] Importantly, considering the influence from real water matrix is an open issue for heavy metal ions detection, river water samples were also tested and successfully measured with the same sensitivity, because all the humic acids/organic matter in the river water were separated/trapped at the bottom

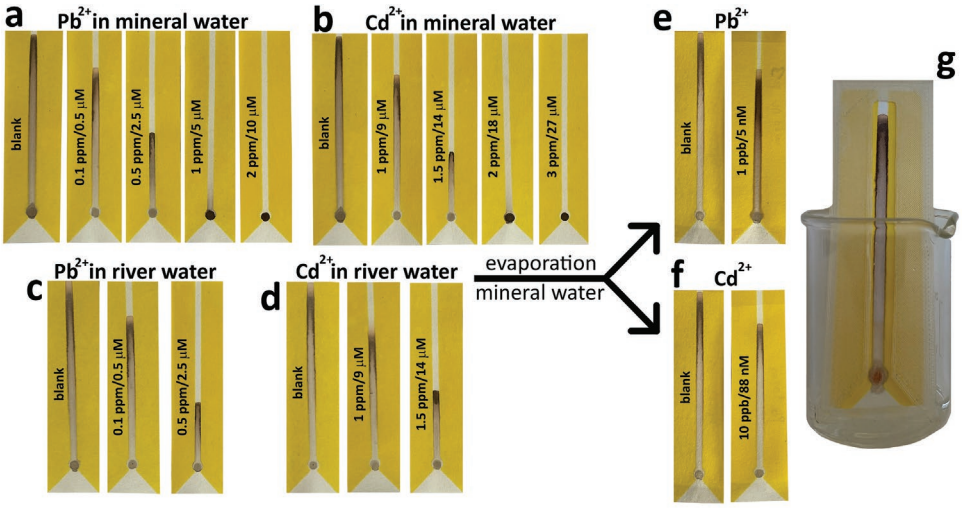

Figure 7. Dose-dependent effect of Pb^{2+} and Cd^{2+} concentration on NGA's flow on the paper after 30 min of analysis. a,b) Pb^{2+} and Cd^{2+} in the presence of different concentrations detected by paper sensor in mineral water. c,d) Pb^{2+} and Cd^{2+} in the presence of different concentrations detected by paper sensor in river water. e,f) Pb^{2+} and Cd^{2+} in the presence of different concentrations detected by paper sensor in mineral water after evaporation. g) The paper sensor in a protective 3D printed case.

© 2022 The Authors. Small published by Wiley-VCH GmbH

16136829, 2022, 33, Downloaded from https://onlinelibrary.wiley.com/doi/10.1002/smll.202201003 by Spanish Cochrane National Provision (Ministerio de Sanidad), Wiley Online Library on [18/10/2022]. See the Terms and Conditions (https://onlinelibrary.wiley.com/terms-and-conditions) on Wiley Online Library for rules of use; OA articles are governed by the applicable Creative Commons License

of the paper-sensor (Figure S20, Supporting Information) and thus not affecting the detection (Figure 7c,d). Therefore, the NGA paper sensor can deliver on-site rigorous and practical water quality control, requiring only the facile evaporation of the water sample, a cup as sample holder, and a 3D printed case (Figure 7g), enabling its straightforward application by untrained users. Such a sensor based on simple operation principles, involving direct use of the nanographene (without any surface modification) and naked-eye detection with few ppb's sensitivity and high selectivity is of particular interest, since such features have not been reported before. Some related sensors rely on chemically functionalized paper with the heavy metal-sensitive β-galactosidase (B-GAL) for the colorimetric visualization of its enzymatic activity inhibition, delivering LoDs of 680 and 180 nM for Pb^{2+} and Cd^{2+}, respectively.[93] In addition, the sensor was similarly sensitive to the much less toxic Cu^{2+} cations (allowance limit of 1.3 ppm). Colorimetric lateral flow sensors, with the use of proteins, antibodies, or metal specific DNA, offered detection of Cd^{2+} at 10 ppb (90 nM)[94] or for Pb^{2+} at 0.5 μm,[95] as the first lower concentrations discernible by the naked eye. It should be also noted that the naked-eye detection via color intensity differences on the test-lines of the strips (especially considering the inaccuracy from different light conditions during testing) is much more challenging than detecting the differences in the distance traveled by the dark colored NGA. We have not identified reports based on this principle, which, along with the previous observations with respect to the current state of the art, underline the effectiveness of the presently developed NGA paper sensor.

3. Conclusion

The present work introduces a design principle leading to recyclable materials for potent and selective heavy metal decontamination, effectively combined with high-performance water-quality monitoring technologies (for mineral, tap, or even complex-matrix samples like river water), using low and ultra-low-cost signal transduction methods. These properties were imprinted by engineering dense and covalent dual functionalization of the graphene backbone with carboxylic groups and nitrogen atoms as multidentate metal traps, accompanied with size confinement that contributed to the material's photoluminescence properties. Carboxylic groups are highly effective coordination ligands for Cd^{2+} and Pb^{2+} cations but are less effective toward coordination of common minerals in drinking water, thus making the reported material a highly selective and efficient sorbent. The carboxyl-nitrogen heterobifunctional and multidentate sites offered antibody-level affinity pockets, forming dark complexes with Cd^{2+} and Pb^{2+} functioning as PL-quenching sensors with LoD of 0.1 and 0.2 nM for Pb^{2+} and Cd^{2+}, respectively, outperforming not only state-of-the-art sensors of this type, but also sensors based on electrochemical signals or operating via exploitation of metal-selective DNA and aptamer strands. The reported design principle could be further expanded for sensing additional analytes, either by modifying the present material (thanks to its abundant carboxyl groups) with other molecules with high affinity for other types of analytes, or by synthesis of new materials bearing such potent, heterobifunctional and multidentate coordination sites as gates for sensitive and selective signal regulation.

Supporting Information

Supporting Information is available from the Wiley Online Library or from the author.

Acknowledgements

The work was supported by the ERDF/ESF project "Nano4Future" (No. CZ.02.1.01/0.0/0.0/16_019/0000754). R.Z. and A.B. acknowledge the funding from the Czech Science Foundation, GA CR–EXPRO, 19-27454X. D.P., L.Z., V.Š., M.L., and V.H. thank the Internal Student Grant Agency of the Palacký University in Olomouc, Czech Republic (IGA_PrF_2022_019). M.O. acknowledges the ERC grant 2D-CHEM, No 683024 from H2020. Operation of XPS and TEM facilities was partly funded by the Research Infrastructure NanoEnviCz, supported by the Ministry of Education, Youth and Sports of the Czech Republic under Project No. LM2018124. N.C. gratefully acknowledges the IKY foundation for the financial support. N.C. and A.B.B. also thank the European Social Fund-ESF (co-financed by Greece and the European Union) through the Operational Programme "Human Resources Development, Education and Lifelong Learning" in the context of the project "Strengthening Human Resources Research Potential via Doctorate Research" (MIS-5000432), implemented by the State Scholarships Foundation (IKY). Ms. Jana Dzíbelová, Ms. Kateřina Roháčová, Mr. Ondřej Tomanec, and Ms. Jana Stráská are acknowledged for TGA analysis, Raman spectroscopy, HR-TEM, and TEM characterization of samples, respectively. Dr. Martin Pykal is acknowledged for the development of the 3D printed cover case and its subsequent manufacturing. Computational resources were supplied by the project "e-Infrastruktura CZ" (e-INFRA CZ LM2018140) supported by the Ministry of Education, Youth, and Sports of the Czech Republic. This work was supported by the Ministry of Education, Youth, and Sports of the Czech Republic through the e-INFRA CZ (ID:90140). ICN2 is funded by CERCA programme, Generalit de Catalunya. Grant SEV-2017-0706 by MCIN/AEI/10.13039/501100011033. The authors also acknowledge the project MAT2017-87202-P funded by MCIN/AEI/10.13039/501100011033 and FEDER Una manera de hacer Europa. R.A.-D. acknowledges funding from the European Union Horizon 2020 Programme under Grant No. 881603 (Graphene Flagship Core 3).

Conflict of Interest

A patent application related to this work is pending.

Data Availability Statement

The data that support the findings will be available in Mendeley at https://www.10.17632/gjr838mv9s.1 following an embargo from the date of publication to allow for commercialization of research findings.

Keywords

carboxylation, heavy metals, nitrogen-doped graphene acid, paper-based sensors, sensing, sorption

Received: February 16, 2022
Revised: March 22, 2022
Published online: July 1, 2022

© 2022 The Authors. Small published by Wiley-VCH GmbH

16136829, 2022, 33, Downloaded from https://onlinelibrary.wiley.com/doi/10.1002/smll.202201003 by Spanish Cochrane National Provision (Ministerio de Sanidad), Wiley Online Library on [18/10/2022]. See the Terms and Conditions (https://onlinelibrary.wiley.com/terms-and-conditions) on Wiley Online Library for rules of use; OA articles are governed by the applicable Creative Commons License

[1] S. Bolisetty, R. Mezzenga, *Nat. Nanotechnol.* **2016**, *11*, 365.
[2] G. L. Sun, E. E. Reynolds, A. M. Belcher, *Nat. Sustainability* **2020**, *3*, 303.
[3] J. O. Nriagu, *Science* **1996**, *272*, 223.
[4] Sustainable Development Knowledge Platform (United Nations), https://sustainabledevelopment.un.org (accessed: March 2022)
[5] {WHO} Fact Sheet on Water: Key Facts, Access to Water, Water and Health, https://water.org/documents/223/FY22_Key_Water.org_facts.pdf (accessed: June 2022).
[6] Water scarcity, https://www.unicef.org/wash/water-scarcity (accessed: March 2022)
[7] J. Filip, J. Kolařík, E. Petala, M. Petr, O. Šráček, R. Zbořil, in *Nanoscale Zerovalent Iron Particles for Environmental Restoration* (Eds: T. Phenrat, G. V. Lowry), Springer, Cham **2019**, pp. 157–199.
[8] T. J. Bandosz, *Activated Carbon Surfaces in Environmental Remediation*, Elsevier, New York **2006**.
[9] L. Xie, Z. Yu, S. M. Islam, K. Shi, Y. Cheng, M. Yuan, J. Zhao, G. Sun, H. Li, S. Ma, M. G. Kanatzidis, *Adv. Funct. Mater.* **2018**, *28*, 1800502.
[10] Y. Peng, H. Huang, Y. Zhang, C. Kang, S. Chen, L. Song, D. Liu, C. Zhong, *Nat. Commun.* **2018**, *9*, 187.
[11] A. A. Uliana, N. T. Bui, J. Kamcev, M. K. Taylor, J. J. Urban, J. R. Long, *Science* **2021**, *372*, 296.
[12] J. Kolařík, A. Bakandritsos, Z. Bad'ura, R. Lo, G. Zoppellaro, Š. Kment, A. Naldoni, Y. Zhang, M. Petr, O. Tomanec, J. Filip, M. Otyepka, P. Hobza, R. Zbořil, *ACS Nano* **2021**, *15*, 3349.
[13] S. Ma, L. Huang, L. Ma, Y. Shim, S. M. Islam, P. Wang, L.-D. Zhao, S. Wang, G. Sun, X. Yang, M. G. Kanatzidis, *J. Am. Chem. Soc.* **2015**, *137*, 3670.
[14] C. W. Abney, J. C. Gilhula, K. Lu, W. Lin, *Adv. Mater.* **2014**, *26*, 7993.
[15] Q. Li, D. Wang, X. Fang, B. Zong, Y. Liu, Z. Li, S. Mao, K. K. Ostrikov, *Chem. Commun.* **2021**, *57*, 1161.
[16] J. Linton, J. S. Yeomans, *Nat. Mater.* **2004**, *3*, 199.
[17] A. D. Pournara, A. Margariti, G. D. Tarlas, A. Kourtelaris, V. Petkov, C. Kokkinos, A. Economou, G. S. Papaefstathiou, M. J. Manos, *J. Mater. Chem. A* **2019**, *7*, 15432.
[18] S.-Y. Ding, M. Dong, Y.-W. Wang, Y.-T. Chen, H.-Z. Wang, C.-Y. Su, W. Wang, *J. Am. Chem. Soc.* **2016**, *138*, 3031.
[19] N. Gogoi, M. Barooah, G. Majumdar, D. Chowdhury, *ACS Appl. Mater. Interfaces* **2015**, *7*, 3058.
[20] Y. Zhang, J. R. Vallin, J. K. Sahoo, F. Gao, B. W. Boudouris, M. J. Webber, W. A. Phillip, *ACS Cent. Sci.* **2018**, *4*, 1697.
[21] X. Shi, W. Gu, W. Peng, B. Li, N. Chen, K. Zhao, Y. Xian, *ACS Appl. Mater. Interfaces* **2014**, *6*, 2568.
[22] X. Niu, Y. Zhong, R. Chen, F. Wang, Y. Liu, D. Luo, *Sens. Actuators, B* **2018**, *255*, 1577.
[23] E. Cho, J. Kim, B. Tejerina, T. M. Hermans, H. Jiang, H. Nakanishi, M. Yu, A. Z. Patashinski, S. C. Glotzer, F. Stellacci, B. A. Grzybowski, *Nat. Mater.* **2012**, *11*, 978.
[24] Z.-Q. Zhou, Y.-P. Liao, J. Yang, S. Huang, Q. Xiao, L.-Y. Yang, Y. Liu, *Spectrochim. Acta, Part A* **2020**, *228*, 117795.
[25] J. Zhou, B. Li, A. Qi, Y. Shi, J. Qi, H. Xu, L. Chen, *Sens. Actuators, B Chem.* **2020**, *305*, 127462.
[26] X. Wang, L. Kong, Y. Gan, T. Liang, S. Zhou, J. Sun, H. Wan, P. Wang, *Anal. Chim. Acta* **2020**, *1131*, 126.
[27] S. Zhu, J. Zhang, X. Liu, B. Li, X. Wang, S. Tang, Q. Meng, Y. Li, C. Shi, R. Hu, B. Yang, *RSC Adv.* **2012**, *2*, 2717.
[28] L. Lu, L. Zhou, J. Chen, F. Yan, J. Liu, X. Dong, F. Xi, P. Chen, *ACS Nano* **2018**, *12*, 12673.
[29] A. Kumar, A. R. Chowdhuri, D. Laha, T. K. Mahto, P. Karmakar, S. K. Sahu, *Sens. Actuators, B* **2017**, *242*, 679.
[30] Y. Liu, Q. Zhou, Y. Yuan, Y. Wu, *Carbon* **2017**, *115*, 550.
[31] C. Liu, X. Chen, B. Zongab, S. Mao, *J. Mater. Chem. A* **2019**, *7*, 6616.
[32] L. Liu, K. Ye, C. Lin, Z. Jia, T. Xue, A. Nie, Y. Cheng, J. Xiang, C. Mu, B. Wang, F. Wen, K. Zhai, Z. Zhao, Y. Gong, Z. Liu, Y. Tian, *Nat. Commun.* **2021**, *12*, 3870.
[33] J. Dong, K. Zhang, X. Li, Y. Qian, H. Zhu, D. Yuan, Q.-H. Xu, J. Jiang, D. Zhao, *Nat. Commun.* **2017**, *8*, 1142.
[34] J. Chen, Q. Huang, H. Huang, L. Mao, M. Liu, X. Zhang, Y. Wei, *Nanoscale* **2020**, *12*, 3574.
[35] Y. Xiang, Y. Lu, *Nat. Chem.* **2011**, *3*, 697.
[36] O. Knopfmacher, M. L. Hammock, A. L. Appleton, G. Schwartz, J. Mei, T. Lei, J. Pei, Z. Bao, *Nat. Commun.* **2014**, *5*, 2954.
[37] Y. Guan, B. Sun, *Microsyst. Nanoeng.* **2020**, *6*, 14.
[38] M. Park, T. S. Seo, *Biosens. Bioelectron.* **2019**, *126*, 405.
[39] E. Vermisoglou, D. Panáček, K. Jayaramulu, M. Pykal, I. Frébort, M. Kolář, M. Hajdúch, R. Zbořil, M. Otyepka, *Biosens. Bioelectron.* **2020**, *166*, 112436.
[40] I. L. Medintz, A. R. Clapp, H. Mattoussi, E. R. Goldman, B. Fisher, J. M. Mauro, *Nat. Mater.* **2003**, *2*, 630.
[41] Q. Li, D. Wang, X. Fang, X. Wang, S. Mao, K. K. Ostrikov, *Adv. Funct. Mater.* **2021**, *31*, 2104572.
[42] J. M. R. Flauzino, E. P. Nguyen, Q. Yang, G. Rosati, D. Panáček, A. G. Brito-Madurro, J. M. Madurro, A. Bakandritsos, M. Otyepka, A. Merkoçi, *Biosens. Bioelectron.* **2022**, *195*, 113628.
[43] K. Hola, Y. Zhang, Y. Wang, E. P. Giannelis, R. Zboril, A. L. Rogach, *Nano Today* **2014**, *9*, 590.
[44] O. Kozák, M. Sudolská, G. Pramanik, P. Cígler, M. Otyepka, R. Zbořil, *Chem. Mater.* **2016**, *28*, 4085.
[45] Q. Wang, S. Zhang, H. Ge, G. Tian, N. Cao, Y. Li, *Sens. Actuators, B* **2015**, *207*, 25.
[46] Lead and Cadmium in Drinking-Water, Background Document for Development of WHO Guidelines for Drinking-Water Quality, https://apps.who.int/iris/handle/10665/75364 (accessed: June 2022).
[47] J. Li, Y. Lu, *J. Am. Chem. Soc.* **2000**, *122*, 10466.
[48] C.-W. Liu, C.-C. Huang, H.-T. Chang, *Anal. Chem.* **2009**, *81*, 2383.
[49] I. L. Medintz, H. T. Uyeda, E. R. Goldman, H. Mattoussi, *Nat. Mater.* **2005**, *4*, 435.
[50] V. Šedajová, A. Bakandritsos, P. Błoński, M. Medveď, R. Langer, D. Zaoralová, J. Ugolotti, J. Dzíbelová, P. Jakubec, V. Kupka, M. Otyepka, *Energy Environ. Sci.* **2022**, *15*, 740.
[51] P. Lazar, R. Mach, M. Otyepka, *J. Phys. Chem. C* **2019**, *123*, 10695.
[52] D. Zaoralová, V. Hrubý, V. Šedajová, R. Mach, V. Kupka, J. Ugolotti, A. Bakandritsos, M. Medved, M. Otyepka, *ACS Sustainable Chem. Eng.* **2020**, *8*, 4764.
[53] X. Wang, C. G. Bazuin, C. Pellerin, *Vib. Spectrosc.* **2014**, *71*, 18.
[54] J. Senthilnathan, C.-C. Weng, J.-D. Liao, M. Yoshimura, *Sci. Rep.* **2013**, *3*, 2414.
[55] G. Socrates, *Infrared and Raman Characteristic Group Frequencies: Tables and Charts*, 3rd ed., Wiley, New York **2021**, p. 332.
[56] J. Oomens, J. D. Steill, *J. Phys. Chem. A* **2008**, *112*, 3281.
[57] D. W. Mayo, F. A. Miller, R. W. Hannah, *Course Notes on the Interpretation of Infrared and Raman Spectra*, Wiley, New York **2004**, p. 222.
[58] P. Yasaei, B. Kumar, R. Hantehzadeh, M. Kayyalha, A. Baskin, N. Repnin, C. Wang, R. F. Klie, Y. P. Chen, P. Král, A. Salehi-Khojin, *Nat. Commun.* **2014**, *5*, 4911.
[59] Y. Hernandez, V. Nicolosi, M. Lotya, F. M. Blighe, Z. Sun, S. De, I. T. McGovern, B. Holland, M. Byrne, Y. K. Gun'Ko, J. J. Boland, P. Niraj, G. Duesberg, S. Krishnamurthy, R. Goodhue, J. Hutchison, V. Scardaci, A. C. Ferrari, J. N. Coleman, *Nat. Nanotechnol.* **2008**, *3*, 563.
[60] M. Bacon, S. J. Bradley, T. Nann, *Part. Part. Syst. Charact.* **2014**, *31*, 415.
[61] M. A. Sk, A. Ananthanarayanan, L. Huang, K. H. Lim, P. Chen, *J. Mater. Chem. C* **2014**, *2*, 6954.
[62] Z. Liu, F. Li, Y. Luo, M. Li, G. Hu, X. Pu, T. Tang, J. Wen, X. Li, W. Li, *Molecules* **2021**, *26*, 3922.
[63] Q. Xue, H. Huang, L. Wang, Z. Chen, M. Wu, Z. Li, D. Pan, *Nanoscale* **2013**, *5*, 12098.

© 2022 The Authors. Small published by Wiley-VCH GmbH

16136829, 2022, 33, Downloaded from https://onlinelibrary.wiley.com/doi/10.1002/smll.202201003 by Spanish Cochrane National Provision (Ministerio de Sanidad), Wiley Online Library on [18/10/2022]. See the Terms and Conditions (https://onlinelibrary.wiley.com/terms-and-conditions) on Wiley Online Library for rules of use; OA articles are governed by the applicable Creative Commons License

[64] M. Fu, F. Ehrat, Y. Wang, K. Z. Milowska, C. Reckmeier, A. L. Rogach, J. K. Stolarczyk, A. S. Urban, J. Feldmann, *Nano Lett.* **2015**, *15*, 6030.
[65] S. Kim, C. M. Park, M. Jang, A. Son, N. Her, M. Yu, S. Snyder, D.-H. Kim, Y. Yoon, *Chemosphere* **2018**, *212*, 1104.
[66] R. G. Pearson, *J. Chem. Educ.* **1968**, *45*, 581.
[67] L.-L. Li, J. Ji, R. Fei, C.-Z. Wang, Q. Lu, J.-R. Zhang, L.-P. Jiang, J.-J. Zhu, *Adv. Funct. Mater.* **2012**, *22*, 2971.
[68] R. Sitko, E. Turek, B. Zawisza, E. Malicka, E. Talik, J. Heimann, A. Gagor, B. Feist, R. Wrzalik, *Dalton Trans.* **2013**, *42*, 5682.
[69] Y. Yu, G. Zhang, L. Ye, *J. Appl. Polym. Sci.* **2019**, *136*, 47318.
[70] M. A. Tofighy, T. Mohammadi, *J. Hazard. Mater.* **2011**, *185*, 140.
[71] X. Guo, B. Du, Q. Wei, J. Yang, L. Hu, L. Yan, W. Xu, *J. Hazard. Mater.* **2014**, *278*, 211.
[72] F. Ge, M.-M. Li, H. Ye, B.-X. Zhao, *J. Hazard. Mater.* **2012**, *211–212*, 366.
[73] Y. Li, J. He, K. Zhang, T. Liu, Y. Hu, X. Chen, C. Wang, X. Huang, L. Kong, J. Liu, *RSC Adv.* **2019**, *9*, 397.
[74] P. Bhunia, G. Kim, C. Baik, H. Lee, *Chem. Commun.* **2012**, *48*, 9888.
[75] M. Nováček, O. Jankovský, J. Luxa, D. Sedmidubský, M. Pumera, V. Fila, M. Lhotka, K. Klímová, S. Matějková, Z. Sofer, *J. Mater. Chem. A* **2017**, *5*, 2739.
[76] G. Zhao, J. Li, X. Ren, C. Chen, X. Wang, *Environ. Sci. Technol.* **2011**, *45*, 10454.
[77] H. Xue, Q. Chen, F. Jiang, D. Yuan, G. Lv, L. Liang, L. Liu, M. Hong, *Chem. Sci.* **2016**, *7*, 5983.
[78] B. Wang, H. Wu, L. Yu, R. Xu, T.-T. Lim, X. W. D. Lou, *Adv. Mater.* **2012**, *24*, 1111.
[79] L. Ma, Q. Wang, S. M. Islam, Y. Liu, S. Ma, M. G. Kanatzidis, *J. Am. Chem. Soc.* **2016**, *138*, 2858.
[80] Z. Tao, Y. Zhou, N. Duan, Z. Wang, *Catalysts* **2020**, *10*, 600.
[81] D. Zhang, M. Zhu, L. Zhao, J. Zhang, K. Wang, D. Qi, Y. Zhou, Y. Bian, J. Jiang, *Inorg. Chem.* **2017**, *56*, 14533.
[82] M. Devi, A. Dhir, C. P. Pradeep, *RSC Adv.* **2016**, *6*, 112728.
[83] A. Shahat, K. T. Kubra, S. Salman, N. Hasan, M. Hasan, *Microchem. J.* **2021**, *164*, 105967.
[84] L. Chen, Y. Lu, M. Qin, F. Liu, L. Huang, J. Wang, H. Xu, N. Li, G. Huang, Z. Luo, B. Zheng, *Sensors* **2020**, *20*, 995.
[85] Y. Zhang, Z. Zhang, D. Yin, J. Li, R. Xie, W. Yang, *ACS Appl. Mater. Interfaces* **2013**, *5*, 9709.
[86] M. Tang, X. Liu, N. Zhang, J. Pang, Y. Zou, F. Chai, H. Wu, L. Chen, *Anal. Methods* **2019**, *11*, 5214.
[87] W.-J. Niu, D. Shan, R.-H. Zhu, S.-Y. Deng, S. Cosnier, X.-J. Zhang, *Carbon* **2016**, *96*, 1034.
[88] L. Tran, S. Park, *Sci. Rep.* **2021**, *11*, 15196.
[89] S. S. Nagarkar, B. Joarder, A. K. Chaudhari, S. Mukherjee, S. K. Ghosh, *Angew. Chem., Int. Ed.* **2013**, *52*, 2881.
[90] B. Wang, P. Wang, L.-H. Xie, R.-B. Lin, J. Lv, J.-R. Li, B. Chen, *Nat. Commun.* **2019**, *10*, 3861.
[91] V. Strauss, J. T. Margraf, C. Dolle, B. Butz, T. J. Nacken, J. Walter, W. Bauer, W. Peukert, E. Spiecker, T. Clark, D. M. Guldi, *J. Am. Chem. Soc.* **2014**, *136*, 17308.
[92] F. Aquino, N. Govind, J. Autschbach, *J. Chem. Theory Comput.* **2010**, *6*, 2669.
[93] S. M. Z. Hossain, J. D. Brennan, *Anal. Chem.* **2011**, *83*, 8772.
[94] A. M. López_Marzo, J. Pons, D. A. Blake, A. Merkoçi, *Biosens. Bioelectron.* **2013**, *47*, 190.
[95] D. Mazumdar, J. Liu, G. Lu, J. Zhou, Y. Lu, *Chem. Commun.* **2010**, *46*, 1416.

© 2022 The Authors. Small published by Wiley-VCH GmbH

16136829, 2022, 33, Downloaded from https://onlinelibrary.wiley.com/doi/10.1002/smll.202201003 by Spanish Cochrane National Provision (Ministerio de Sanidad), Wiley Online Library on [18/10/2022]. See the Terms and Conditions (https://onlinelibrary.wiley.com/terms-and-conditions) on Wiley Online Library for rules of use; OA articles are governed by the applicable Creative Commons License